Scanning ultrasound improves memory and enhances functional outcomes in Alzheimer's mice in the absence of amyloid-β reduction

Gerhard Leinenga[1], Xuan Vinh To[2,3], Liviu-Gabriel Bodea[1], Jumana Yousef[4,5], Gina Richter-Stretton[1], Tishila Palliyaguru[1], Antony Chicoteau[1], Laura Dagley[4,5], Fatima Nasrallah[2,3], and Jürgen Götz[1,*]

[1]Clem Jones Centre for Aging Dementia Research, Queensland Brain Institute, The University of Queensland, Brisbane, QLD, Australia; [2]Queensland Brain Institute, The University of Queensland, Brisbane, QLD, Australia; [3]Centre for Advanced Imaging, The University of Queensland, Brisbane, QLD, Australia [4]Proteomics Facility, The Walter and Eliza Hall Institute of Medical Research, Melbourne, VIC, Australia; [5]Department of Medical Biology, The University of Melbourne, Parkville, VIC, 3052, Australia

*Correspondence: j.goetz@uq.edu.au

Abstract

A prevalent view in treating age-dependent disorders including Alzheimer's disease (AD) is that the underlying pathology must be targeted for cognitive improvements. In contrast, we report here that repeated scanning ultrasound treatment at 1 MHz, can ameliorate memory deficits without reducing amyloid-β (Aβ) burden in the APP23 mouse model of AD. No microbubbles were used to achieve blood-brain barrier opening. Intriguingly, the treatment was less effective at 286 kHz, which is within the frequency range currently explored in transcranial clinical trials in AD patients. Functional magnetic resonance imaging and quantitative proteomics revealed that ultrasound differentially induced long-term functional improvements in the brain. Together, our data suggest a dose-dependent effect of ultrasound on functional read-outs and a dissociation of cognitive improvement and Aβ clearance, with important implications for AD trial design.

Teaser

Amyloid removal is not required for therapeutic effects of ultrasound in AD mice and is a function of the ultrasound frequency

MAIN TEXT

Introduction

Alzheimer's disease (AD) is the leading cause of disability in the aging population, accounting for up to 80% of all cases. The overarching histopathological feature is that two key molecules, amyloid-β (Aβ) and tau, form insoluble aggregates. These develop into microscopically visible brain lesions known as Aβ plaques and tau-containing neurofibrillary tangles (*1*). Both Aβ and tau

dysfunction are believed to initiate and drive the degenerative process in AD, leading to a progressive impairment of memory, reasoning, and social engagement (*2*). A routinely used system to model aspects of AD and other dementias is transgenic mice (*3*). Aβ plaque formation, together with memory impairment, has been reproduced in several transgenic lines including APP23 mice. This strain expresses the human amyloid precursor protein (APP) together with the K670N/M671L pathogenic mutation present in familial cases of AD (*4*).

Given the challenges of developing effective pharmacological treatments for AD and other brain diseases, alternative strategies including low-intensity focused ultrasound (FUS) are currently being explored (*5*). At high intensity, ultrasound is being used as a focused, incisionless, FDA-approved surgical tool for ablating brain tissue and thereby treating diseases such as essential tremor and tremor-dominant Parkinson's disease (*6*). At low intensity, ultrasound is being investigated as neuromodulatory and/or blood-brain barrier (BBB) opening tool in multiple animal species and human study participants (*5, 6*).

To achieve its bio-effects, ultrasound induces mechanical effects, which can be categorized into acoustic radiation forces and cavitation. Thermal effects are largely negligible at low ultrasound intensities. When ultrasound interacts with intravenously injected microbubbles (FUS^{+MB}, used by us in a scanning mode, SUS^{+MB}) cavitation is augmented, leading to BBB opening. This causes an uptake of blood-borne factors, some of which with therapeutic effects (*6*). Several research groups have thereby been able (i) to reduce amyloid plaque load in AD mouse models (such as APP23 mice), without co-injecting exogenous drugs (*7-9*), and (ii) to improve memory functions (*7-9*). Activation of dormant microglia by unidentified blood-borne factors taken up through an opened BBB has been identified as underlying mechanism, with Aβ being taken up into and cleared by microglial lysosomes. This robust Aβ clearance was assumed to be the reason for the improved memory functions.

Ultrasound has also been explored without delivering microbubbles (SUS^{only}), a modality whereby cavitation effects are largely absent and the effects of ultrasound are neuromodulatory, utilizing its radiation forces. Such a treatment proved insufficient to clear Aβ (*10*). Given that low-intensity ultrasound is increasingly being explored as a novel treatment option in AD patients, either with (*11-13*) or without microbubbles (*14*), we asked whether the SUS^{only} paradigm could improve spatial memory in APP23 mice, and whether Aβ reductions are required as one would assume because Aβ is the culprit causing the cognitive impairments in the first place. Here, we explored two frequencies, 1 MHz (in the following termed HighF), routinely used in mice (*8, 15*) and via intracranially implanted transducers in AD patients (*13*), as well as 286 kHz (in the following termed LowF), a frequency within a range (210-650 kHz) at which transcranial human FUS^{+MB} treatments are generally performed (*11, 12*), because at 1 MHz, attenuation and aberration of the human skull are too high to achieve safe and efficacious bio-effects.

Interestingly, we found that repeated HighF treatments of APP23 mice, unlike LowF treatments, improved spatial memory in the active place avoidance (APA) paradigm. Contrary to the prevalent view that Aβ pathology (in addition to tau) drives the degenerative process and that for cognitive functions to improve, Aβ needs to be cleared (or its production reduced), we found that the memory improvements occurred in the absence of Aβ reductions. Resting-state functional magnetic resonance imaging (rsfMRI) connectivity studies in AD patients have shown that there is a dysfunction in network-level organization of the brain, including the default mode, salience, and limbic networks (*16, 17*). We therefore also investigated whether ultrasound treatment achieves a long-lasting modulation of these dysfunctional brain networks and therefore represents an alternative therapeutic approach to AD. Our results revealed that SUS^{only}, particularly at the 1 MHz frequency, induced long-term structural and functional changes in neurons and their connections, as revealed by rsfMRI and quantitative proteomics. Together, our data suggest a dissociation of cognitive improvement and Aβ clearance, with important implications for AD

treatment strategies. They further suggest that the current clinical trials may not use optimal ultrasound parameters, with our data providing a new handle for ultrasound treatment optimization.

Results

High-frequency SUS improves spatial memory performance

To investigate low-intensity ultrasound in the absence of microbubbles (i.e., no opening of the BBB) in an animal model of AD, we used two types of transducers, one operating at 1 MHz and a second at 286 kHz ultrasound, both achieving a similar derated (internal) pressure of 0.57 MPa (Fig. 1A). The study comprised four treatment arms: untreated wild-type mice, and APP23 mice that either received 8 weekly treatments at 1 MHz in a SUS^{only} scanning mode (HighF), or 286 kHz in a SUS^{only} scanning mode (LowF) and sham (i.e. with the mice being anesthetized and placed under the transducer but without receiving an ultrasound treatment) (Fig. 1B). Prior to the first treatment the mice underwent a 5-day spatial memory and learning assessment in the APA test, followed by an allocation to the treatment arms based on their performance. Following treatment, the mice were retested using the 5-day APA spatial memory testing paradigm, then underwent an fMRI assessment, after which they were sacrificed and brains dissected for analysis, including label-free quantitative proteomics (Fig. 1B).

More specifically, we first examined 11 month-old APP23 mice and their wild-type littermates in the APA test, a hippocampus-dependent spatial learning paradigm in which the animals must use visual cues in order to learn to avoid a shock zone located in a rotating arena (Fig. 2A). This test is more suitable to probe memory functions than the Morris water maze, as aged mice are poor swimmers. The mice were first habituated to the arena in one 5-minute session the day before the first training day. The APA test then consisted of five training days with a single 10-minute training session each day.

In this first APA for group assignment, a two-way mixed repeated-measures ANOVA based on the number of shocks that were received revealed a significant effect of day of testing, indicating that learning had occurred (($F_{4,188}$) = 8.96, $p < 0.0001$). There was also a significant effect of genotype, with APP23 mice receiving more shocks than their wild-type littermates (($F_{1,47}$) = 19.47, $p < 0.0001$) (Fig. 2B). Similarly, based on the measure of time to the first entry of the shock zone, there was a significant effect of day, with mice showing longer latencies to the first entrance as the number of training days increased (($F_{4,188}$) = 19.79, $p < 0.0001$). Wild-type mice exhibited longer latencies to enter the shock zone over the days of testing and there was a significant effect of genotype on time to first entry (($F_{1.47}$) = 13.13, $p < 0.0001$) (Fig. 2C). APP23 mice had an increased number of entries to the shock zone (($F_{1,47}$) = 18.11, $p < 0.0001$) (Fig. 2D) and maximum time of avoidance of the shock zone (($F_{1,47}$) = 6.33, $p < 0.0001$) (Fig. 2E). They also performed significantly worse on the measures "time to second entry" (($F_{1,47}$) = 24.16, $p < 0.0001$) (Fig. 2F), but not "proportion of time spent in the quadrant opposite to the shocked quadrant" (Fig. 2G). As the APA performance of the APP23 mice varied significantly, they were assigned to each of the four treatment groups based on matching performance in terms of the number of shocks received on day 5 of the APA to reduce any differences in performance between treatment groups (Fig. 2H).

Before retesting in the APA, mice were treated once a week for 8 weeks with either 1 MHz ultrasound (HighF), 286 kHz frequency ultrasound (LowF) or sham (sham) treatment. For the retest, the shock zone was shifted by 180°, the cues in the room were changed, and the arena was rotated in the opposite direction (Fig. 2I). To perform well in the retest, the mice needed to update their spatial learning in order to learn the new shock zone location, which requires significant cognitive flexibility. A two-way ANOVA with group as a between-subjects factor and

day as a repeated measures factor revealed a significant effect of ultrasound treatment group on number of shocks received (($F_{3,48}$) = 11.27, p < 0.0001) (Fig. 2J). Follow-up multiple comparisons tests showed that HighF mice received significantly fewer shocks than sham mice on days 4 (p =0.004) and 5 (p = 0.008) (Fig. 2J). LowF mice did not show a significant improvement in spatial learning ability compared to sham-treated mice (Fig. 2J). There was no significant effect of ultrasound treatment on time to first shock, which increased over day of training for all groups and revealed a trend towards an effect of the ultrasound treatment (($F_{3,48}$) = 2.36, p = 0.08) on time to first entry into the shock zone, with a follow-up multiple comparisons test showing that ultrasound-treated mice had a longer latency to enter the shock zone on day 5 of the APA task (p = 0.035) (Fig. 2K). There was a significant effect of ultrasound treatment on number of entries (($F_{3,48}$)=8.23, p=0.0002*)* with a follow-up multiple comparisons test showing that HighF mice performed significantly better than sham mice on days 4 (p=0.03) and 5 (p=0.026) (Fig. 2L). There was no significant effect of ultrasound treatment on the maximum time spent avoiding the shock zone (Fig. 2M). However, there was a significant effect of group on the time to the second entry to the shock zone (($F_{3,48}$) = 12.03, p<0.0001) and here, both the LowF and HighF groups showed a benefit with the LowF group showing improvements on day 3 (p=0.027) and HighF mice showing improvement on day 4 of the test (Holm-Sidak multiple comparisons test; p=0.01) (Fig. 2N). There was no effect of group on the time the mice spent in the opposite quadrant to the shock zone (Fig. 2O). The number of shocks received on day 5 of the APA revealed that HighF mice received 43% fewer shocks than sham-treated APP23 mice (Holm-Sidak multiple comparisons test; p =0.004) (Fig. 2P). Together, these results demonstrate that APP23 mice exhibited an improvement in spatial memory when treated with HighF ultrasound, with LowF ultrasound only resulting in slight improvements.

Improved memory functions occur in the absence of reductions in amyloid plaques and Aβ levels

We next examined whether the ultrasound treatments might reduce Aβ levels in brain by first performing Campbell-Switzer silver staining for plaques (Fig. 3A-D). This revealed no reduction in the total plaque area when the ultrasound treatment groups were compared to the sham-treated controls (Fig. 3E). We calculated the percentage area occupied by plaque for the cortex, in 5-10 sections per mouse, assessing plaque burden in a one-in-eight series of sections along the rostral-caudal axis starting from the anterior commissure and ending at the ventral hippocampus. There were no statistically significant differences when comparing sham and ultrasound treatment following a one-way ANOVA (($F_{2,36}$)=1.87, p=0.17). A t-test to compare HighF to sham revealed a slight increase in plaque burden, but this was not statistically significant (p=0.16) (Fig. 3E). When the number of plaques with an area larger than 20 μm^2 was quantified and normalized to the area of the cortex, no differences in plaque number were revealed (*(*$F_{2,36}$) = 0.97, p=0.39) (Fig. 3F).

As an additional assessment of amyloid load, we sequentially extracted the cortices of the mice to obtain a detergent-soluble fraction (SDC) containing soluble proteins and a detergent-insoluble fraction containing insoluble proteins (guanidine HCl) and measured the levels of the Aβ species, $A\beta_{40}$ and $A\beta_{42}$, by enzyme-linked immunosorbent assay (ELISA). Our results revealed no significant differences in the levels of $A\beta_{42}$ in the insoluble fraction (Fig. 3G) (one-way ANOVA, p=0.59) but a significant difference in the soluble fraction (p=0.001) (Fig. 3H). Levels of $A\beta_{40}$ were not different between the treatment groups for the insoluble fraction (p=0.71) (Fig. 3I) or the soluble fraction (Fig. 3J) (p=0.51). Together with the analysis of amyloid plaques, these findings reveal that improved memory function in the SUS^{only}-treated APP23 mice occurred in the absence of amyloid reductions.

Ultrasound improves brain network connectivity as measured with rsfMRI

AD is associated with a widespread loss of both intra- and inter-network correlations as revealed by rsfMRI (*18*), which has been reproduced in amyloid-depositing transgenic strains (*19*). We found in SUS^{only}-treated APP23 mice that stimulus-evoked cortical activation did not differ across all treatment conditions, and had no effect on the extent or strength of cortical activation in response to mild forepaw electrical stimulation. However, we found increased rsfMRI connectivity in the hippocampal and salience networks in the HighF group compared to both sham and LowF mice suggestive of enhanced interaction between these specific areas in the brain. These findings indicate that the HighF treatment specifically improves connectivity in memory-related networks compared to other treatments and controls.

Interestingly, negative correlations were observed between the somatosensory network and the striatal and hippocampal networks in the HighF versus LowF and HighF versus sham groups (Fig. 4A-F). Negative correlations in resting state networks are an underexplored area yet evidence suggests that these opposing and anti-correlating regions can be interpreted as regions with opposing functions as the brain drifts between internal and external mental states (*20*). The enhanced negative correlations in the HighF group may indicate better switching ability across different mental states in these mice.

Effect of ultrasound on brain microstructure

We next performed structural MRI and diffusion MRI imaging to investigate changes in brain volume and microstructure (Fig. 5A). Compared to the sham group, both the LowF and HighF groups had decreased local tissue volume (TBM). The decreased local tissue volume in the treated groups was also associated with increased isotropic diffusion fraction in the same area predominantly in the neocortical areas and the anterior hippocampus (Fig. 5B). Both treated groups showed increased ventricle volumes being compared to sham which was consistent with the increased isotropic diffusion volume fractions seen in both treatment conditions (flSO) (Fig. 5B). For neurite-orientation density and dispersion index (NODDI), the HighF treatment group showed a decreased orientation dispersion index (ODI) and neurite density index (NDI) mainly in the cortex (Fig. 5B). The LowF group had increased ODI in the white matter tracts (Fig. 5C). Together, the decreased ODI and NDI in the context of treatment in APP-related pathology may be associated with the enhanced neurocognition observed.

We also performed dynamic contrast-enhanced MRI to measure cerebral blood volume; however, fitting of the Dynamic Susceptibility Contrast (DSC) data resulted in a large fraction of the datasets having cerebral blood volume (CBV) maps with predominantly negative values, even with leakage correction, indicating significant levels of BBB leakage in these animals. This supports the notion that the BBB is impaired under many neurodegenerative conditions (*21*). Although DSC is not optimized for the detection of BBB integrity, we classified the animals with datasets that feasible CBV maps after DSC model fitting as having “intact BBB” and those without feasible CBV maps as having “leaky BBB”, as a gross proxy estimation of the proportion of animals in each group with leaky versus non-leaky BBB. Sham mice had 5 mice with “leaky BBB” (55% of the mice) and 4 with “intact BBB”, LowF had 7 mice with “leaky BBB” (78% of the mice) and 2 mice with “intact BBB” and the HighF group had 8 mice with “leaky BBB” (88% of the mice) and 2 with “intact BBB”. A Chi-square test showed a statistically insignificant difference in the ratio of animals with “leaky” and “non-leaky” BBB across the treatment groups ($p=0.8$). This suggests that BBB integrity was not adversely impacted by the SUS treatment.

Ultrasound treatment alters the proteome of APP23 mice in a dose-dependent manner

Given that ultrasound exerts pleiotropic effects on brain tissue, as reported recently in senescent mice that lack an amyloid pathology (*22*), we performed label-free quantitative proteomic analysis on cortical lysates of APP23 mice subjected to either HighF, LowF or sham treatment. Principal component analysis (PCA) (Fig. 6A) revealed that the proteomes of ultrasound-treated mice grouped together, away from the proteome of sham-treated mice, and that the HighF mice showed a relatively larger magnitude of changes compared to the LowF animals, reflecting the differences seen in spatial memory functions.

Out of a total of 2,115 proteins identified by our proteomic pipeline, differential analysis revealed 15 upregulated proteins common to both the HighF and LowF mice compared to sham, and none that was downregulated in both treatments when compared to sham (Fig. 6B). The same analysis identified 18 upregulated proteins and 16 downregulated proteins that were specific to the HighF group compared with the sham mice, and only 2 upregulated and 2 downregulated proteins in the LowF group compared with sham-treated mice (Fig 6B). Heatmap (Fig. 6C) and volcano plot representations of the dysregulated proteins (Fig. 6D) revealed similar up- or down-regulation effects induced by the HighF versus sham treatment (32 significantly upregulated and 21 significantly downregulated proteins in volcano plots), whereas the LowF effect was, as expected, less impactful, but markedly skewed towards upregulation of protein expression (17 up- and 2 downregulated proteins vs sham) (Fig. 6D).

Our proteomic analysis led to the identification of four expression clusters based on their treatment-effect trajectory that were differentially expressed between the groups (Fig. 7). The first cluster (n=155) was characterized by increased expression in the LowF group that was further enhanced by the high intensity treatment (Fig. 7A). Cluster 1 was characterized by differential expression specific to Golgi vesicle transport, and establishment of protein localization to the membrane or to the cell periphery. Members of this cluster included SNX1 (member of the sorting nexin family), RAB5A (GTPase involved in endosome transport and found within different cellular components, including axon terminal boutons), and STX1b (involved in exocytosis of synaptic vesicles). Cluster 2 (n=186) (Fig. 7B) was composed of proteins with upregulated expression following LowF treatment, but a more moderate expression increase induced by the HighF treatment. This cluster was enriched in proteins associated with exocytosis, and axonal genesis and development. Interestingly, proteins belonging to this cluster included MAP1A and MAP6 (microtubule-associated proteins that contribute to axonal development and stabilization). Other members of the cluster were STX1A, SNX4 and CALM3, having functions related to exocytosis. Cluster 3 (n=173) (Fig. 7C) was represented by proteins that showed a steep downregulation starting with the LowF treatment, but a moderate decrease after HighF treatment of mice. The cluster was also found to be associated with axonogenesis and axonal development, as well as with vesicle organization. Proteins which were dysregulated in this cluster were associated with the action potential (GPD1L, GNA11, GNAQ) and localization of vesicles (RAB7A, DCTN2, MAP2). Finally, cluster 4 (n=147) (Fig. 7D) was represented by proteins that showed a marked intensity-dependent downregulation of their expression. The functions associated with this cluster were represented by histone modification and response to hypoxia. Proteins which were downregulated in this cluster are represented by ACTB, SFPQ, NOS1 and MECP2.

Together, these findings not only indicate that the HighF mice show a relatively larger magnitude of changes to the proteome compared to the LowF and sham-treated animals, as expected, but they also provide a molecular explanation for the improvements seen in the spatial memory paradigm and functional magnetic resonance imaging in the HighF experimental group compared to the LowF group and sham-treated mice.

Discussion

In AD, memory deficits are assumed to be a consequence of the accumulation of Aβ (and tau) aggregation (*23, 24*). Previously, we had revealed in APP23 mice with an Aβ pathology that ultrasound application in combination with the intravenous injection of microbubbles (SUS^{+MB}) both safely and transiently disrupted the BBB; this led to amyloid clearance through increased microglial internalization, as well as memory improvements (*8, 25, 26*). The assumption at the time was that memory improvements or functional improvements are contingent on reducing Aβ.

Here, we show that therapeutic ultrasound applied without microbubbles (SUS^{only}), but with parameters shown previously to improve cognition in aged wild-type mice (*22*), improved memory function, increased neuronal connectivity and induced long-lasting changes in the proteome in APP23 mice, without lowering Aβ levels (Fig. 8). More specifically, two months of weekly ultrasound treatments led to improvements in spatial learning and memory, and increased functional connectivity as measured by rsfMRI. This was accompanied by changes to the neuronal proteome and distinct signaling pathways, as well as changes to brain structure. Interestingly, this was not related to amyloid clearance, as shown by determining amyloid plaque load histologically, and levels of soluble and insoluble Aβ by ELISA.

The improvements in memory and functional connectivity observed in the ultrasound-treated mice may be due to changes in synaptic protein expression and alterations in tissue microstructure, blood flow, and free water diffusion resulting from the ultrasound treatment. It has been shown previously that levels of synaptic proteins can predict the rate of cognitive decline in human AD patients when measured post mortem (*27*) or with positron emission tomography (PET) (*28*). Interestingly, the reduced brain volume detected by T2-weighted MRI in the ultrasound-treated mice is consistent with other studies that have shown significantly increased brain volume loss in AD patients in clinical trials (*29*). It has been speculated that plaque removal may explain the volume loss, but this is unlikely the to be the reason given the small volume of brain taken up by plaques compared to the magnitude of changes found on MRI. How changes to brain microstructure detected in our study relate to changes in cognition could be subject of further studies, but we note that it occurred with both LowF and HighF ultrasound stimulation, although the latter had a greater effect on memory.

The SUS^{only} neuromodulation employed here improves memory in AD mice and in senescent wild-type mice (*22*). This finding has some similarities to other brain stimulation methods (such as repetitive transcranial magnetic stimulation) which have been found to improve memory function in healthy humans, specifically by stimulating regions of the prefrontal cortex (*30*). There is also evidence that brain stimulation can improve cognitive abilities in patients with AD, and clinical trials are underway (*31*). Ultrasound is likely to have both overlapping and distinct mechanisms of action to electrical and magnetic stimulation, as it exerts a mechanical force on brain tissue and mediates its effects through the activation of mechanosensitive ion channels on neurons and glia (*32, 33*).

To the best of our knowledge, our study for the first time reveals frequency-specific effects of ultrasound on cognition and connectivity in mice. 1 MHz (HighF) was more effective than 286 kHz (LowF) in our study, possibly because of the increased acoustic radiation force exerted for the HighF condition. Other studies reported that higher frequency ultrasound has larger neurostimulatory effects on neurons in the retina (*34*). It is believed that mechanical stimulation of neurons has a role in the effects of ultrasound, with multiple mechanosensitive ion channels expressed on neurons that can respond to ultrasound (*5*). Magnetic resonance acoustic radiation force imaging (MR-ARFI) has shown that ultrasound at both 0.22 and 1 MHz causes micrometer-scale displacements in brain tissue (*34*). Additionally, is has been demonstrated that the radiation force is proportional to absorption and increases with frequency, with higher frequency ultrasound leading to more absorption and larger displacements in brain tissue (*35, 36*).

We found that ultrasound stimulation caused changes to the neuronal proteome, with four dysregulated clusters relating to synaptic vesicle function and exocytosis, axonogenesis and

neuronal signaling. Along with improved cognitive function, we also detected changes in the functional connectivity as measured by MRI. Interestingly, reduced functional connectivity by fMRI was found in 5xFAD mice (*37*) and in a rat model of AD (*38*). We revealed that in addition to cellular level alterations induced by ultrasound, brain circuits may also be affected as reflected by changes in functional connectivity. Others have shown long-lasting effects in primates (for 45 minutes) after stimulation with 500 kHz ultrasound (*39*). It was further found that FUS alters neuronal circuits and behaviors in macaques for up to one hour after stimulation (*40*). The long-term changes in functional connectivity occurring in our study two weeks after the last ultrasound treatment may be a consequence of alterations in the neuronal proteome that may underlie the improvements in cognitive function.

APP23 mice are characterized by premature lethality during the first 4-6 months of age which presents a challenge to breeding planning (*41*). A limitation of our study therefore is that the experimental groups were comprised of 75% male and 25% female mice; however, the ratio of males to females was the same for all treatment groups. Our study could therefore not ascertain a possible difference between male and female mice in their response to ultrasound. A second potential limitation of our study is that the treatment protocol with weekly treatments for two months was designed to be similar to a clinically relevant protocol. We did not assess the effect of ultrasound in real-time during ultrasound neurostimulation as we were interested in the amelioration of clinical symptoms rather than studying the online effects of ultrasound, and the immediate effects of ultrasound application or other timepoints remains to be determined.

In an AD context, ultrasound has previously been used to achieve concomitant BBB opening (FUS^{+MB}) in mouse models (*7, 8, 42*), and in a small number of AD patients (*11*). Also, a clinical trial has been conducted in AD patients using ultrasound shockwaves (*14*). For nearly a century, the scientific community has been aware that ultrasound can impact neuronal activity. As reviewed recently, we have now gained a better understanding of how to use this knowledge to modulate neurons to achieve therapeutic outcomes as reviewed recently (*5*). The current study adds to the changes that have been reported to be elicited by ultrasound stimulation, applied to a model of AD. We found that SUS^{only} differentially induced long-term functional improvements in the brain, as shown by quantitative proteomics and functional magnetic resonance imaging. Importantly, these improvements occurred in the absence of Aβ reductions (Fig. 8). Our study therefore implies that cognitive improvement and Aβ clearance can be dissociated, with important implications for treatment strategies. We conclude that our findings are relevant for the rapidly growing space of therapeutic ultrasound, whether used as a neuromodulatory or BBB-opening tool for drug delivery.

Materials and Methods

Study design

APP23 mice express human APP751 with the Swedish double mutation (KM670/671NL) under the control of the neuron-specific mThy1.2 promoter. As the mice age, they exhibit memory deficits and amyloid plaque formation (*41*). In this study, 12 months-old APP23 mice were assigned to three treatment groups: sham (N = 12), 1 MHz ultrasound (N = 12, HighF), and 286 kHz ultrasound (N=11, LowF). Assignment to treatment groups was based on matching performance of spatial memory (number of shocks) on day 5 of the APA test. APP23 mice were ranked from those receiving the fewest shocks to those receiving the most shocks on day 5 and were assigned to the three APP23 ultrasound treatment groups in rank order. A group of wild-type mice (N = 12) was included as fourth group. Following eight weekly treatments, mice underwent

an APA re-test over five days, followed by an MRI analysis and the collection of brains for a proteomic, biochemical and histological analysis (Fig.1).

Animal ethics

All animal experimentation was approved by the Animal Ethics Committee of the University of Queensland (approval number QBI/554/17).

Ultrasound equipment

For the 286 kHz ultrasound application, a H-117 transducer was used (Sonic Concepts Bothell WA USA). This transducer has a diameter of 64 mm, a radius of curvature of 63 mm, and an internal opening of 20 mm diameter. For the 1 MHz ultrasound application, an integrated focused ultrasound system was used (Therapy Imaging Probe System, TIPS, Philips Research). This system consists of an annular array transducer with a natural focus of 80 mm, a radius of curvature of 80 mm, a spherical shell of 80 mm with a central opening of 31 mm diameter, a 3D positioning system, and a programmable motorized system to move the ultrasound focus in the x and y planes to cover the entire brain area. A coupler mounted to the transducer was filled with degassed water and placed on the depilated head of the mouse with ultrasound gel for coupling, to ensure propagation of the ultrasound to the brain.

Ultrasound application

Mice were anesthetized with ketamine (90 mg/kg) and xylazine (6 mg/kg), and the hair on the head was shaved and depilated. The parameters for ultrasound delivery for the LowF condition were: 286 kHz center frequency, 0.57 MPa peak rarefactional pressure in situ (as estimated by needle hydrophone measurements obtained in water and assuming negligible attenuation through the skull), 10 Hz pulse repetition frequency (PRF), 10 ms pulse length (PL), and a 6 s sonication time per spot. Ultrasound was generated by a H-117 model transducer (Sonic Concepts) that was 64 mm diameter with a 63.2 mm radius of curvature and a 22 mm inner opening. The -6 dB focal zone was 6 mm (lateral) x 39.5 mm (axial). A motorized positioning system moved the focus of the transducer array to four spots spaced 6 mm apart in relation to the skull such that the entire brain of the mouse was exposed to ultrasound. The HighF condition was: 1 MHz centre frequency, 0.7 MPa peak rarefactional pressure (as estimated by needle hydrophone measurements in water for device calibration), 10 Hz PRF, 10 ms PL, and 6 s sonication per spot (Fig. 1). Ultrasound was generated by an eight-element annular array (TIPS system, Philips Research) with a diameter of 80 mm with an inner hole of 32 mm, an 80 mm radius of curvature. The focal zone of the array (-6 dB) was an ellipse of approximately 1.5 mm × 1.5 mm × 12 mm. The TIPS motorized positioning system moved the focus of the transducer array in a grid with 1.5 mm between individual sites of sonication so that ultrasound was delivered sequentially to the entire brain. The pressure level inside the brain was adjusted to be the equivalent for the HighF and LowF ultrasound groups (0.57 MPa derated) accounting for the higher, estimated 18% attenuation of 1 MHz ultrasound by the mouse skull (*43*).

Assessment of amyloid plaques

For the assessment of amyloid plaque load, an entire one-in-eight series of coronal brain sections taken from the start of the anterior commissure to the ventral hippocampus of one hemisphere at 40 µm thickness was stained using the Campbell-Switzer silver staining protocol that stains both compact plaques and more diffuse amyloid fibrils but we did not distinguish these types in our

analysis (*8*). Stained sections were mounted onto microscope slides and imaged with a 10x objective on a Metafer bright-field VSlide scanner (MetaSystems) using Zeiss Axio Imager Z2. Analysis of amyloid plaque load was performed using FIJI on all stained sections using ImageJ. A region of interest (ROI) was drawn around the cortex, and automated thresholding for plaques was applied to the ROIs, with the fill holes and despeckle functions applied to allow all plaques to be counted. A size threshold of 50 μm^2 was applied to determine the number of plaques per area. No size thresholding was applied for the calculation of total plaque burden.

Enzyme-linked immunosorbent assay for Aβ

Frozen cortices were homogenized in 10 volumes of a solution containing 1% sodium deoxycholate in 0.1M phosphate buffered saline with complete protease inhibitors, and homogenized by passing through 19 and 27 gauge needles. The samples were then centrifuged at 21,000×g for 90 min at 4 °C. The supernatant was retained as the detergent-extracted soluble Aβ fraction. The remaining pellets were resuspended in 10 volumes of 5 M guanidine HCl, sonicated, and centrifuged at 21,000×g for 30 min at 4 °C. The resultant supernatant was retained as the guanidine-extracted insoluble Aβ fraction. The concentrations of $A\beta_{40}$ and $A\beta_{42}$ were determined in brain lysates using ELISA kits according to the manufacturer's instructions (human $A\beta_{40}$ and $A\beta_{42}$ brain ELISA, Invitrogen).

Active place avoidance test

The APA task is a test of hippocampus-dependent spatial learning. We used a repeated APA paradigm, where mice were tested in the APA one time and the performance of each mouse was used to assign that mouse to one of four treatment groups. This was done by ranking all the mice based on their performance and assigning them to the four groups in order so that the APA performance of each treatment group was the same. Following this, mice received either sham, HighF or LowF treatment. Three days after the last treatment, they were retested to assess whether there was an improvement in APA performance. For each APA test, APP23 mice and non-transgenic littermate controls were tested over 6 days in a rotating elevated arena (Bio-Signal group) that had a grid floor and a 32-cm-high clear plastic circular fence enclosing a total diameter of 77 cm. High-contrast visual cues were present on the walls of the testing room. The arena and floor were rotated at a speed of 0.75 rpm, with a mild shock (500 ms, 60 Hz, 0.5 mA) being delivered through the grid floor each time the animal entered a 60-degree shock zone, and then every 1,500 ms until it left the shock zone. The shock zone was maintained at a constant position in relation to the room. Recorded tracks were analyzed with Track Analysis software (Bio-Signal). A habituation session was performed 24 h before the first training session during which the animals were allowed to explore the rotating arena for 5 min without receiving any shocks. A total of five training sessions were held on consecutive days, one per day with a duration of 10 min. After day 5 of the first APA (test), APP23 mice were divided into four groups with mice matched so that the performance (number of shocks) of the four groups of mice on day 5 of the task was the same, for the retest. Following eight once-a-week sham or ultrasound treatments, the mice underwent the APA test again (reversal learning). The retest was held in the same room as the initial test. However, the shock zone was switched to the opposite side of the arena, the visual cues were replaced with different ones, and the platform was rotated clockwise rather than counterclockwise. The number of shocks, numbers of entries to the shock zone, time to first entry, time to second entry, and proportion of time spent in the opposite quadrant to the shock zone were compared over the days of testing.

Magnetic resonance imaging

Mice were imaged on a 9.4T (Bruker Biospin) MRI scanner between 8 and 12 days after the final (8th) high, low or sham treatment. Deep anesthesia was induced with 3% isoflurane in a 60/40 mixture of air/O_2 at 1 l/min; the isoflurane concentration was reduced to 1.5–2 % for the remaining animal preparation time. Anesthetized mice were placed on the MRI-compatible cradle in a head-first, prone position and the head was fixed using ear bars and a bite bar to avoid movement. An intraperitoneal (i.p.) catheter was inserted and fixed temporarily for the infusion of medetomidine (Domitor, Pfizer) (*44*). A 30-gauge tail vein catheter was inserted into a lateral tail vein for infusion of contrast agent (Magnevist, 0.5 mmol/kg). Subdermal electrodes were inserted near the 2nd and 4th digits on the left forepaw for mild electrical stimulations, which were delivered by a current source (Isostim A320, World Precision Instrument). The animals were monitored for respiration rate, pattern, and stability and rectal temperature (target 37 ± 0.5 °C) using an MRI-compatible rodent physiological monitoring system (Model 1030, SA Instruments).

Following proper positioning of the mouse inside the scanner magnet, an i.p bolus dose of 0.05 mg/kg medetomidine was given and continuous sedation was maintained with continuous medetomidine i.p infusion at 0.1 mg/kg/h. The isoflurane concentration was lowered gradually and maintained at 0.5% throughout the remainder of the experiment. T2-weighted, diffusion, BOLD and contrast-enhanced scans were obtained. The total time under anesthesia was approximately 2.5 h. At the end of the scan, an i.p bolus dose of 1.25 mg/kg atipemazole (for medetomidine reversal) was given and the animals were kept on a heated pad and monitored for recovery.

The sequence parameter details for the T2-weighted (T2w) structural, stimulus-evoked and resting-state functional, and multi-shell diffusion scans have been described previously (*45*). Briefly, T2w structural MRI scans were taken with a Turbo Rapid Acquisition with Refocused Echoes (TurboRARE) sequence with TR/TE = 7200/39 ms and a resolution of 0.1 × 0.1 × 0.3 mm. Stimulus-evoked and resting-state functional MRI scans were acquired with a 2D gradient-echo echo-planar-imaging (GE-EPI) sequence with TR/TE = 1000/14 ms, flip angle = 70°, and spatial resolution of 0.3 × 0.3 × 0.6 mm.

A Dynamic Susceptibility Contrast (DSC) sequence was acquired using a 2D gradient-echo echo-planar-imaging (GE-EPI) sequence with the following parameters: matrix size = 64 × 64, FOV = 19.2 × 19.2mm, 17 slices of 0.7 mm thickness and 0.1 mm slice gaps; giving an output spatial resolution of 0.3 × 0.3 × 0.8mm, TR/TE = 550/14 ms, flip angle = 35°, bandwidth = 3125 Hz/pixel, fat suppression = ON, FOV saturation (covering the head tissue inferior to the mouse's brain) = ON, and navigator pulses = ON. The DSC sequence was started and allowed to run for 60 s before the contrast agent bolus was delivered; the DSC sequence was scanned with 982 volumes.

Magnetic resonance imaging analysis

The preprocessing and image registration of the structural, diffusion, and functional MRI images were done based on detailed procedures as previously described (*46*). Briefly, structural images were corrected for bias field inhomogeneity and then normalized to a common space by an iterative image registration-template creation procedure, and the Jacobian images were used for a tensor-based morphometry analysis of structural differences. Diffusion MRI data were distortion and motion corrected, and fitted for the NODDI model, and also spatially normalized using a similar procedure to structural image. Orientation dispersion index (ODI), neurite density index (NDI), and fraction of isotropic diffusion (fISO) were obtained from the multi-shell diffusion MRI data. Functional MRI data were distortion and motion corrected, high-pass filtered at 0.01 Hz and also spatially normalized before being analyzed through a data-driven group independent component analysis (group ICA) using group information-guided independent component

analysis (GIG-ICA) (*47*). Independent components were selected and grouped into larger networks (*45*). DSC MRI data were processed and spatially normalized to a common space using a process similar to that used for functional MRI data. Dynamic Susceptibility Contrast (DSC) data were fitted using the Dynamic Susceptibility Contrast MRI toolbox (https://github.com/marcocastellaro/dsc-mri-toolbox) with semi-automatic aterial input function selection and blood-brain barrier leakage correction (*48*).

SWATH mass spectrometry

To identify changes in protein abundance following 1 MHz or 286 kHz ultrasound treatments compared to sham, total cortical protein extracts from 10-12 mice per group were analyzed by SWATH-MS. Briefly, 45 µg of protein from each sample was diluted in triethylammonium bicarbonate buffer and subsequently reduced with DTT, followed by alkylation with iodoacetamide. Samples were then digested with 80 ng of trypsin overnight, after which they underwent a buffer exchange to be resuspended in 2% acetonitrile, 0.1% formic acid. In order to form a unique peptide library, 5 µg from each of the samples were first pooled together and then fractionated via high pH reversed-phase high-performance liquid chromatography to form 18 fractions that were then analyzed via data-dependent acquisition (IDA).

For IDA, the sample (10 µL) was injected onto a reverse-phase peptide trap for pre-concentration and desalted with loading buffer, at 5 µL/min for 3 min. The peptide trap was then switched into line with the analytical column. Peptides were eluted from the column using a linear solvent gradient from mobile phase A: mobile phase B (95:5) to mobile phase A: mobile phase B (65:35) at 300 nL/min over a 60 min period. After peptide elution, the column was cleaned with 95% buffer B for 6 min and then equilibrated with 95% buffer A for 10 min before next sample injection. The reverse phase nanoLC eluent was subject to positive ion nano-flow electrospray analysis in an information dependant acquisition mode (IDA). In the IDA mode a TOF-MS survey scan was acquired (*m/z* 350-1500, 0.25 s) with the 20 most intense multiply charged ions (2+ - 5+; exceeding 200 counts per s) in the survey scan sequentially subjected to MS/MS analysis. MS/MS spectra were accumulated for 100 ms in the mass range *m/z* 100–1800 with rolling collision energy.

Data independent acquisition (SWATH) was performed as follows: Sample (10 µL, ~ 2 µg) was injected onto a reverse-phase peptide trap for pre-concentration and desalted with loading buffer, at 5 µL/min for 3 min. The peptide trap was then switched into line with the analytical column. Peptides were eluted from the column using a linear solvent gradient from mobile phase A: mobile phase B (95:5) to mobile phase A: mobile phase B (65:35) at 300 nL/min over a 60 min period. After peptide elution, the column was cleaned with 95% buffer B for 6 min and then equilibrated with 95% buffer A for 10 min before next sample injection. The reverse phase nanoLC eluent was subject to positive ion nano-flow electrospray analysis in a data independent acquisition (SWATH). In SWATH mode, first a TOFMS survey scan was acquired (*m/z* 350-1500, 50 ms) and then, the 100 predefined *m/z* ranges were sequentially subjected to MS/MS analysis. MS/MS spectra were accumulated for 30 ms in the mass range *m/z* 350-1500.

Database searches for IDA data were performed as follows: The data files generated by IDA-MS analysis were searched with ProteinPilot (v5.0) (Sciex) using the ParagonTM algorithm in thorough mode. *Mus musculus* 'uniprot-mus_musculus containing 17,119 proteins on July 4th 2022, was used for searching the data. Carbamidomethylation of Cys residues was selected as a fixed modification. An Unused Score cut-off was set to 1.3 (95% confidence for identification), and global protein FDR of 1%.

For SWATH extraction and quantitation, the local ion library was constructed using the 2D-IDAs. The library contains 4,448 proteins. Ion library and SWATH data files were imported into PeakView (v2.2) (Sciex). Protein peak area information in SWATH data were extracted

using PeakView (v2.2) with the following parameters: Top 6 most intense fragments of each peptide were extracted from the SWATH data sets (75 ppm mass tolerance, 10 min retention time window). Shared and modified peptides were excluded. After data processing, peptides (max 100 peptides per protein) with confidence ≥99% and FDR ≤1% (based on chromatographic feature after fragment extraction) were used for quantitation.

Bioinformatics analysis of SWATH-MS data

Data processing and analysis were performed using R (version 4.2.1). Proteins that were identified by two or more peptides were used in the analysis pipeline. A total of **2,115** proteins were included in the analysis. Protein intensities were $\log_2$-transformed. Normalization based on groups was performed using RUVIIIC (v. 1.0.19). Invariant proteins in all conditions ($p > 0.5$), with a coefficient of variation (CV%) < 2%, were chosen as negative controls for RUVIIIC normalization. Differential analysis was performed using limma (v. 3.52.4). A protein was determined to be significantly differentially expressed if the fold change was ≥ 1.5 or ≤ 0.5 and the false discovery rate (FDR) was ≤ 5% after Benjamini–Hochberg (H-B) correction.

Clustering analysis was performed based on mixed-effects models with Gaussian variables and a non-parametric cubic splines estimation approach implemented in TMixClust R package (v.1.18.0) GO (gene ontology) analysis and KEGG (Kyoto Encyclopedia of Genes and Genomes) pathways analysis were performed using clusterProfiler R-package (v. 4.4.4).

Statistical analysis

Statistical analyses were conducted with Prism 9 software (GraphPad). Values were always reported as mean ± SEM. One-way ANOVA followed by the Holm-Sidak multiple comparisons test, or *t* test was used for all comparisons except APA analyses where two-way ANOVA with day as a repeated measures factor and group as a between subjects factor was performed, followed by the Holm-Sidak multiple comparisons test for simple effects to compare group performances on different days. The model assumption of equal variances was tested by Brown-Forsyth or Bartlett tests, and the assumption of normality was tested by Kolmogorov-Smirnov tests and by inspecting residuals with QQ plots. All observations were independent, with allocation to groups based on APA where mice were ranked on performance and assigned to one of the three groups (HighF, LowF, sham) in order of number of shocks on day 5 ranked from most to least shocks.

Spatially normalized MRI outputs, including Jacobian Index (obtained from T2w structural MRI image registration procedure), NODDI metrics (ODI, NDI, and fISO) and group ICA independent components' spatial maps were analyzed as 2 sample t-tests using permutation inference for the General Linear model as implemented in FSL's randomize (*49*). The number of permutations was set to 10000, as recommended by a prior study (*50*). The resulting statistical maps were corrected for multiple comparisons with mass-based FSL's Threshold-free Cluster enhancement (TFCE) (*51*) and thresholded at $p < 0.05$ (two-tailed). One and two-samples statistical tests were conducted on individual level independent components' time courses using GIFT's Mancovan toolbox for IC-IC functional network connectivity (FNC) and corrected for multiple comparisons with False Discovery Rate at q-value < 0.05 for one-sample t-tests and q-value < 0.1 for two-sample t-tests.

References

1. M. Goedert, M. G. Spillantini, A century of Alzheimer's disease. *Science* **314**, 777-781 (2006).
2. C. R. Jack, Jr., Advances in Alzheimer's disease research over the past two decades. *Lancet Neurol* **21**, 866-869 (2022).
3. P. Padmanabhan, J. Götz, Clinical relevance of animal models in aging-related dementia research. *Nat Aging* **3**, 481-493 (2023).
4. C. Sturchler-Pierrat *et al.*, Two amyloid precursor protein transgenic mouse models with Alzheimer disease-like pathology. *Proc Natl Acad Sci U S A* **94**, 13287-13292 (1997).
5. D. G. Blackmore, D. Razansky, J. Götz, Ultrasound as a versatile tool for short- and long-term improvement and monitoring of brain function. *Neuron*, (2023).
6. Y. Meng, K. Hynynen, N. Lipsman, Applications of focused ultrasound in the brain: from thermoablation to drug delivery. *Nat Rev Neurol* **17**, 7-22 (2021).
7. J. F. Jordao *et al.*, Amyloid-beta plaque reduction, endogenous antibody delivery and glial activation by brain-targeted, transcranial focused ultrasound. *Exp Neurol* **248**, 16-29 (2013).
8. G. Leinenga, J. Götz, Scanning ultrasound removes amyloid-beta and restores memory in an Alzheimer's disease mouse model. *Science translational medicine* **7**, 278ra233 (2015).
9. Y. Shen *et al.*, Ultrasound with microbubbles improves memory, ameliorates pathology and modulates hippocampal proteomic changes in a triple transgenic mouse model of Alzheimer's disease. *Theranostics* **10**, 11794-11819 (2020).
10. G. Leinenga, W. K. Koh, J. Götz, Scanning ultrasound in the absence of blood-brain barrier opening is not sufficient to clear beta-amyloid plaques in the APP23 mouse model of Alzheimer's disease. *Brain Res Bull* **153**, 8-14 (2019).
11. N. Lipsman *et al.*, Blood-brain barrier opening in Alzheimer's disease using MR-guided focused ultrasound. *Nature communications* **9**, 2336 (2018).
12. Y. Meng *et al.*, Resting state functional connectivity changes after MR-guided focused ultrasound mediated blood-brain barrier opening in patients with Alzheimer's disease. *NeuroImage* **200**, 275-280 (2019).
13. S. Epelbaum *et al.*, Pilot study of repeated blood-brain barrier disruption in patients with mild Alzheimer's disease with an implantable ultrasound device. *Alzheimers Res Ther* **14**, 40 (2022).
14. R. Beisteiner *et al.*, Transcranial Pulse Stimulation with Ultrasound in Alzheimer's Disease-A New Navigated Focal Brain Therapy. *Adv Sci (Weinh)* **7**, 1902583 (2020).
15. R. M. Nisbet *et al.*, Combined effects of scanning ultrasound and a tau-specific single chain antibody in a tau transgenic mouse model. *Brain* **140**, 1220-1230 (2017).
16. J. J. Palop, J. Chin, L. Mucke, A network dysfunction perspective on neurodegenerative diseases. *Nature* **443**, 768-773 (2006).
17. J. Zhou, W. W. Seeley, Network dysfunction in Alzheimer's disease and frontotemporal dementia: implications for psychiatry. *Biol Psychiatry* **75**, 565-573 (2014).
18. M. R. Brier *et al.*, Loss of intranetwork and internetwork resting state functional connections with Alzheimer's disease progression. *J Neurosci* **32**, 8890-8899 (2012).
19. J. Grandjean *et al.*, Complex interplay between brain function and structure during cerebral amyloidosis in APP transgenic mouse strains revealed by multi-parametric MRI comparison. *NeuroImage* **134**, 1-11 (2016).
20. X. V. To, V. Vegh, F. A. Nasrallah, Towards data-driven group inferences of resting-state fMRI data in rodents: Comparison of group ICA, GIG-ICA, and IVA-GL. *J Neurosci Methods* **366**, 109411 (2022).
21. M. D. Sweeney, Z. Zhao, A. Montagne, A. R. Nelson, B. V. Zlokovic, Blood-Brain Barrier: From Physiology to Disease and Back. *Physiol Rev* **99**, 21-78 (2019).

22. D. G. Blackmore *et al.*, Low-intensity ultrasound restores long-term potentiation and memory in senescent mice through pleiotropic mechanisms including NMDAR signaling. *Mol Psychiatry* **26**, 6975-6991 (2021).
23. D. J. Selkoe, J. Hardy, The amyloid hypothesis of Alzheimer's disease at 25 years. *EMBO Mol Med* **8**, 595-608 (2016).
24. J. C. Polanco *et al.*, Amyloid-beta and tau complexity - towards improved biomarkers and targeted therapies. *Nat Rev Neurol* **14**, 22-39 (2018).
25. G. Leinenga, W. K. Koh, J. Götz, A comparative study of the effects of Aducanumab and scanning ultrasound on amyloid plaques and behavior in the APP23 mouse model of Alzheimer disease. *Alzheimers Res Ther* **13**, 76 (2021).
26. G. Leinenga *et al.*, Transcriptional signature in microglia isolated from an Alzheimer's disease mouse model treated with scanning ultrasound *Bioeng Transl Med*, (2022).
27. E. Bereczki *et al.*, Synaptic proteins predict cognitive decline in Alzheimer's disease and Lewy body dementia. *Alzheimer's & dementia : the journal of the Alzheimer's Association* **12**, 1149-1158 (2016).
28. A. P. Mecca *et al.*, In vivo measurement of widespread synaptic loss in Alzheimer's disease with SV2A PET. *Alzheimer's & dementia : the journal of the Alzheimer's Association* **16**, 974-982 (2020).
29. F. Barkhof, D. S. Knopman, Brain Shrinkage in Anti-beta-Amyloid Alzheimer Trials: Neurodegeneration or Pseudo-atrophy? *Neurology*, (2023).
30. B. Luber, S. H. Lisanby, Enhancement of human cognitive performance using transcranial magnetic stimulation (TMS). *NeuroImage* **85 Pt 3**, 961-970 (2014).
31. A. Menardi, L. Dotti, E. Ambrosini, A. Vallesi, Transcranial magnetic stimulation treatment in Alzheimer's disease: a meta-analysis of its efficacy as a function of protocol characteristics and degree of personalization. *J Neurol* **269**, 5283-5301 (2022).
32. S. Yoo, D. R. Mittelstein, R. C. Hurt, J. Lacroix, M. G. Shapiro, Focused ultrasound excites cortical neurons via mechanosensitive calcium accumulation and ion channel amplification. *Nature communications* **13**, 493 (2022).
33. S. J. Oh *et al.*, Ultrasonic Neuromodulation via Astrocytic TRPA1. *Curr Biol* **30**, 948 (2020).
34. M. D. Menz *et al.*, Radiation Force as a Physical Mechanism for Ultrasonic Neurostimulation of the Ex Vivo Retina. *J Neurosci* **39**, 6251-6264 (2019).
35. Y. Hertzberg *et al.*, Ultrasound focusing using magnetic resonance acoustic radiation force imaging: application to ultrasound transcranial therapy. *Medical physics* **37**, 2934-2942 (2010).
36. M. A. Phipps *et al.*, Considerations for ultrasound exposure during transcranial MR acoustic radiation force imaging. *Scientific reports* **9**, 16235 (2019).
37. S. R. Kesler, P. Acton, V. Rao, W. J. Ray, Functional and structural connectome properties in the 5XFAD transgenic mouse model of Alzheimer's disease. *Netw Neurosci* **2**, 241-258 (2018).
38. E. Munoz-Moreno, R. Tudela, X. Lopez-Gil, G. Soria, Early brain connectivity alterations and cognitive impairment in a rat model of Alzheimer's disease. *Alzheimers Res Ther* **10**, 16 (2018).
39. F. Munoz *et al.*, Long term study of motivational and cognitive effects of low-intensity focused ultrasound neuromodulation in the dorsal striatum of nonhuman primates. *Brain stimulation* **15**, 360-372 (2022).
40. L. Verhagen *et al.*, Offline impact of transcranial focused ultrasound on cortical activation in primates. *eLife* **8**, (2019).
41. L. M. Ittner *et al.*, Dendritic function of tau mediates amyloid-beta toxicity in Alzheimer's disease mouse models. *Cell* **142**, 387-397 (2010).

42. K. Xhima *et al.*, Ultrasound delivery of a TrkA agonist confers neuroprotection to Alzheimer-associated pathologies. *Brain*, (2021).
43. J. J. Choi, M. Pernot, S. A. Small, E. E. Konofagou, Noninvasive, transcranial and localized opening of the blood-brain barrier using focused ultrasound in mice. *Ultrasound in medicine & biology* **33**, 95-104 (2007).
44. F. A. Nasrallah, H. C. Tay, K. H. Chuang, Detection of functional connectivity in the resting mouse brain. *NeuroImage* **86**, 417-424 (2014).
45. X. V. To, F. A. Nasrallah, A roadmap of brain recovery in a mouse model of concussion: insights from neuroimaging. *Acta neuropathologica communications* **9**, 2 (2021).
46. X. V. To, F. A. Nasrallah, Multi-modal magnetic resonance imaging in a mouse model of concussion. *Sci Data* **8**, 207 (2021).
47. Y. Du, Y. Fan, Group information guided ICA for fMRI data analysis. *NeuroImage* **69**, 157-197 (2013).
48. J. L. Boxerman, K. M. Schmainda, R. M. Weisskoff, Relative cerebral blood volume maps corrected for contrast agent extravasation significantly correlate with glioma tumor grade, whereas uncorrected maps do not. *AJNR Am J Neuroradiol* **27**, 859-867 (2006).
49. A. M. Winkler, G. R. Ridgway, M. A. Webster, S. M. Smith, T. E. Nichols, Permutation inference for the general linear model. *NeuroImage* **92**, 381-397 (2014).
50. D. A. Dickie *et al.*, Permutation and parametric tests for effect sizes in voxel-based morphometry of gray matter volume in brain structural MRI. *Magnetic resonance imaging* **33**, 1299-1305 (2015).
51. S. M. Smith, T. E. Nichols, Threshold-free cluster enhancement: addressing problems of smoothing, threshold dependence and localisation in cluster inference. *NeuroImage* **44**, 83-98 (2009).

Acknowledgments

Funding: We acknowledge support from the Estate of Dr. Clem Jones, the State Government of Queensland (DSITI, Department of Science, Information Technology and Innovation), the National Health and Medical Research Council of Australia (GNT1176326, GNT1145580 and GA39196), the Alzheimer's Association (Chicago) grant 22-AAIIA-965230, and the Terry and Maureen Hopkins Foundation to J.G. L.G.B is the recipient of a Dementia Australia Foundation Mid-Career Research Fellowship.

Acknowledgements: We thank members of our team (Drs Rachel de las Heras and Jae Song) as well as Rowan Tweedale for critical reading of our manuscript.

Author contributions: The study was designed by GL and JG. The experiments were performed by GL, XVT, GR-S and TS. The data were analyzed by GL, XVT, LGB, JY, AC and LD. The paper was written by GL, L-GB, FN and JG. Funding was provided by JG.

Competing interests: The authors declare no conflict of interest.

Data and materials availability: The data will be made available upon reasonable request.

Figures legends

Figure 1.

Study design. (A) APP23 mice aged 11 months were treated with scanning ultrasound, of 1 MHz (HighF) or 286 kHz (LowF) of the same pressure accounting for the higher attenuation of high frequency ultrasound. Exposure of the whole brain was achieved by treating a 5x6 grid of spots with the high frequency device, and 4 spots with the low frequency device, taking into account the different -6 dB widths of the ultrasound focus at HighF (1 MHz, 1.5mm) versus LowF (286 kHz, 6 mm). (B) APP23 mice and their wild-type (WT) littermates were tested in the active place avoidance (APA) test over 5 days of training. APP23 mice then received eight once-per-week ultrasound treatments with either a high frequency or low frequency device, controls received a sham treatment consisting of anesthesia and being placed under the ultrasound transducer, but it was not turned on. WT mice were sham treated. Three days after the last ultrasound treatment, mice were tested again in the APA test in which the extra-maze cues were changed, the shock zone was placed in the opposite quadrant, and the arena rotated in a different direction. Between 2 and 7 days after the conclusion of the APA mice received magnetic resonance imaging (MRI) scans and were sacrificed at the conclusion of the scans.

Figure 2.

Improved spatial memory in APP23 mice in response to SUS^{only} at 1 MHz (HighF) compared to 286 kHz (LowF). (A) Schematic of the arena for the APA test. APP23 mice show impaired performance compared to their WT littermates on the measure (B) number of shocks, (C) on time to first entry of the shock zone, APP23 and WT mice performed similarly, (D) on Number of entries, and (E) maximum time avoidance, and (F) time to second entry to the shock zone, APP23 mice were impaired compared to wild-type littermates, (G) but not time spent in the opposite quadrant of the shock zone. (Two-way ANOVA, * = APP23 $p<0.05$ compared to WT). (H) All mice were ranked based on their performance on the last day (day 5) of the APA and were allocated to groups based on matching performance to receive 1 MHz ultrasound (HighF), 286 kHz ultrasound (LowF) or sham treatment. Following eight ultrasound treatments, mice were retested in the APA with the shock zone location, extramaze cues and direction of arena rotation altered (I). There were significant differences between the treatment groups, such that compared to sham-treated APP23 mice, HighF-ultrasound treated APP23 mice and sham-treated WT mice received fewer shocks (J), had an increased time to first entry on day 5 (K), had reduced number of entries to the shock zone on day 4 and day 5 (L), however maximum time of avoidance did not differ between the groups (M). On the measure time to second entry HighF-ultrasound treated mice showed improved performance on day 4 of the test (N). Ultrasound treatment did not affect proportion of time in the opposite quadrant to the shock zone (O). (P) HighF-treated APP23 mice received significantly fewer shocks on day 5 of the APA retest compared to sham-treated APP23 mice. Two-way ANOVA with follow-up Holm-Sidak test, # $p<0.05$ high frequency compared to sham, * $p<0.05$ WT compared to sham, ^ $p<0.05$ low frequency compared to sham.

Figure 3.

Repeated SUS^{only} treatments at either 1 MHz (HighF) or 286 kHz (LowF) does not reduce plaque burden and amyloid levels. (A) A one-in-eight series of free-floating sections were stained for amyloid plaques with the Campbell-Switzer silver staining method which stains both diffuse and compact plaques equally well. Plaque burden and number of large plaques were analyzed by automated thresholding in ImageJ. Scale bar 1mm. (B) Plaque burden and

morphology appeared similar between the three groups of sham-treated APP23 mice. Scale bar: 100µm. (C) HighF-treated APP23 mice, and (D) LowF-treated mice. (E) Plaque burden expressed as % area was not significantly different between the three groups (one-way ANOVA p=0.16). There was no difference in the number of large plaques per area (F). Cortical tissue was sequentially lysed to generate a detergent soluble (SDC: sodium deoxycholate) fraction and a detergent-insoluble (GuHCl: guanidine hydrochloride fractions) Enzyme-linked immunosorbency assays (ELISAs) for $A\beta_{40}$ and $A\beta_{42}$ found there was no difference in the detergent insoluble $A\beta_{42}$ levels (G), but that the detergent-soluble $A\beta_{42}$ was higher in the high frequency ultrasound treated group (H). Levels of $A\beta_{40}$ were not different between the groups in the detergent insoluble (I) or detergent soluble fraction (J). Box and whisker plots range and median plotted.

Figure 4.

Group averaged resting-state functional MRI functional connectivity. Color scaled by Z test statistics; non-black cells were defined as component-component connectivity deemed statistically significant. One sample t-tests, corrected for multiple comparison correction with False Discovery Rate, thresholded at $Q < 0.05$. Red–Yellow cells: positive correlation. Blue–Green cells: negative correlation. Average resting state functional connectivity for selected ROIs for (A) Sham-treated APP23 mice, (B) LowF-treated APP23 mice, (C) HighF-treated APP23 mice. No significant differences in functional connectivity were found when comparing the LowF- and sham-treated APP23 mice (D); however, HighF-treated APP23 mice showed significant differences in functional connectivity when compared to sham-treated APP23 mice (E), and when compared to LowF-treated APP23 mice (F).

Figure 5.

Changes to brain morphometry and NODDI diffusion measures by group. (A) Time-course of MRI and anesthesia. (B,C) Diffusion MRI reveals structural changes to the brain following HighF (B) and LowF ultrasound treatment (C). Red-yellow voxels show significant increase comparing treatment to Sham, and blue-green voxels indicate significant reduction when comparing ultrasound treatment to Sham. Tensor-based morphometry (TBM) visualized voxels that underwent statistically significant changes indicative of volumetric effects in HighF-treated APP23 mice. Neurite orientation dispersion and density imaging (NODDI) revealed changes in neurite density index (NDI), orientation dispersion index (ODI), and isotropic diffusion volume fraction (fISO) obtained from the diffusion model fitting. Similar changes were found in the LowF ultrasound-treated group. 2 samples t-test results, implemented as randomized test of General Linear Model; statistical maps were corrected for multiple comparisons with Threshold-free Cluster Enhancement (TFCE) at P value < 0.05 (two-tailed). ODI = Orientation Dispersion Index, NDI = Neurite Density Index, fISO = isotropic diffusion volume fraction. Red anatomical orientation indicators: L = Left, R = Right.

Figure 6.

Proteomic analysis of the cortex of APP23 mice subjected to either HighF, LowF or Sham treatment reveal treatment-dependent changes. (A) Principal component analysis (PCA) reveals the presence of a Sham cluster independent of ultrasound treated samples, that show higher similarity, with both HighF and LowF ultrasound treatments clustering together. (B) Upset plot revealing the shared and unique number of proteins that were significantly upregulated (left) or downregulated (right) when compared between treatment regimes. (C) Heatmap of the top significant proteins (n=59) grouped by ultrasound treatment regime. (D) Volcano plot of

differentially expressed proteins, displaying fold change (logFC, $\log_2$ scale) and *P* values ($-\log_{10}$ scale) between cuprizone HighF-treated vs Sham-treated controls (top) and LowF-treated versus Sham-treated controls (top).

Figure 7.

Bioinformatic analysis of proteomic data set identifies four dysregulated clusters that varies with treatment. Analysis of the proteomic data identifies expression patterns (left), the top significant biological processes (middle) and expression networks (right) induced by the HighF and LowF ultrasound treatment. (A) Cluster 1 shows an ultrasound treatment-dependent increase in expression of proteins related with the Golgi vesicle transport, such as sortin nexin 1 (SNX1). (B) Cluster 2 is defined by an ultrasound treatment-dependent increase in expression which is similar in HighF and LowF groups. The cluster is having exocytosis as top functional hit, represented by syntaxin 1a (STX1A). (C) Cluster 3 shows an ultrasound treatment-dependent decrease in protein abundance, expressed similarly in HighF and LowF that is associated with the biology of the axons. (D) Cluster 4 presents a decrease in proteins that varies between HighF and LowF treatment and that associates with the histone modification functional network.

Figure 8.

Summary scheme. Scanning ultrasound without microbubbles (SUS) at 1 MHz (HighF) and to some extent, 286 kHz (LowF) improves memory, enhances functional connectivity and alters the proteome in Alzheimer's disease mice in the absence of amyloid reduction.

Figure 1

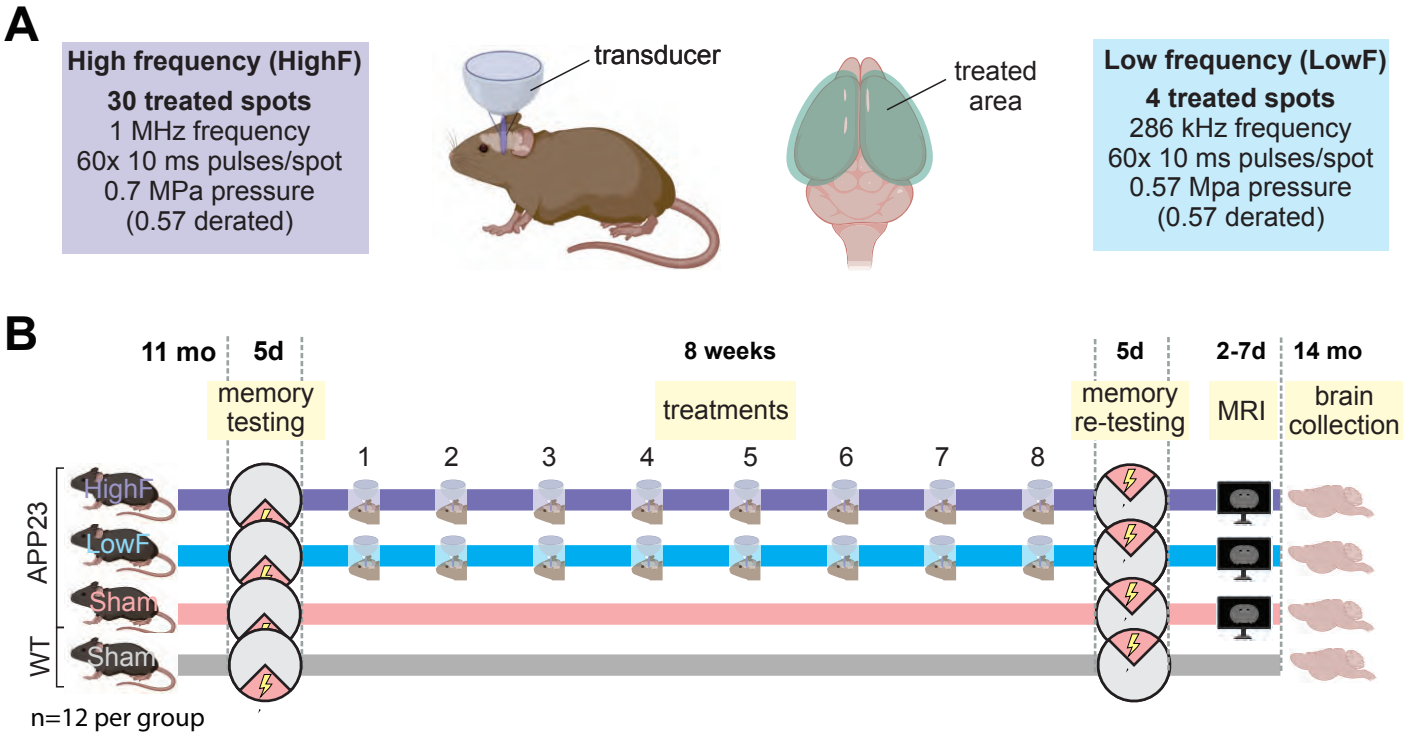
A
High frequency (HighF)
30 treated spots
1 MHz frequency
60x 10 ms pulses/spot
0.7 MPa pressure
(0.57 derated)
transducer
treated area
Low frequency (LowF)
4 treated spots
286 kHz frequency
60x 10 ms pulses/spot
0.57 Mpa pressure
(0.57 derated)
B
11 mo
5d
8 weeks
5d
2-7d
14 mo
memory testing
treatments
memory re-testing
MRI
brain collection
1
2
3
4
5
6
7
8
APP23
WT
HighF
LowF
Sham
Sham
n=12 per group

Figure 2

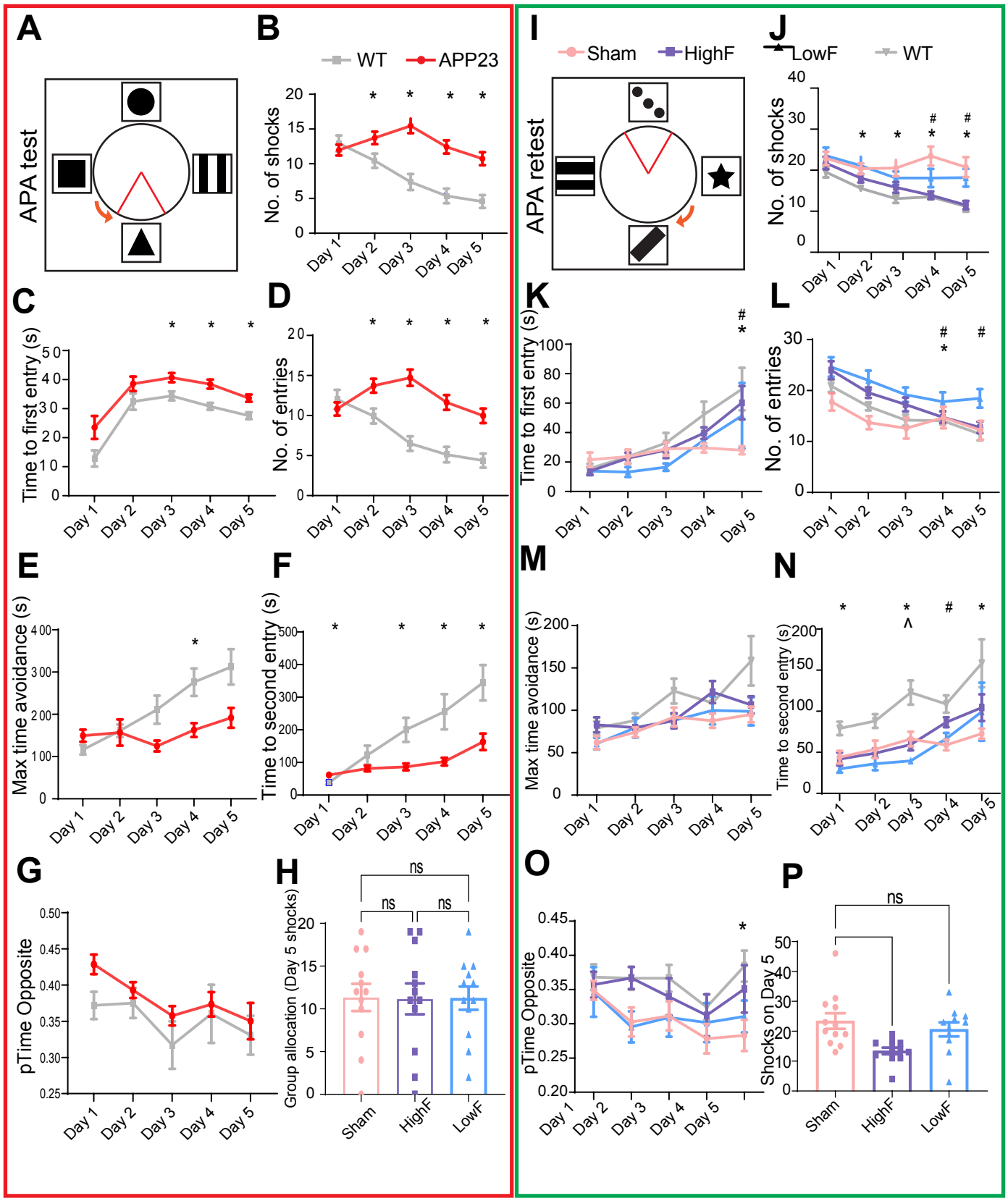
A
APA test
B
WT
APP23
No. of shocks
Day 1
Day 2
Day 3
Day 4
Day 5
C
Time to first entry (s)
D
No. of entries
E
Max time avoidance (s)
F
Time to second entry (s)
G
pTime Opposite
H
Group allocation (Day 5 shocks)
ns
Sham
HighF
LowF
I
APA retest
J
K
L
M
N
O
P
Shocks on Day 5

Figure 3

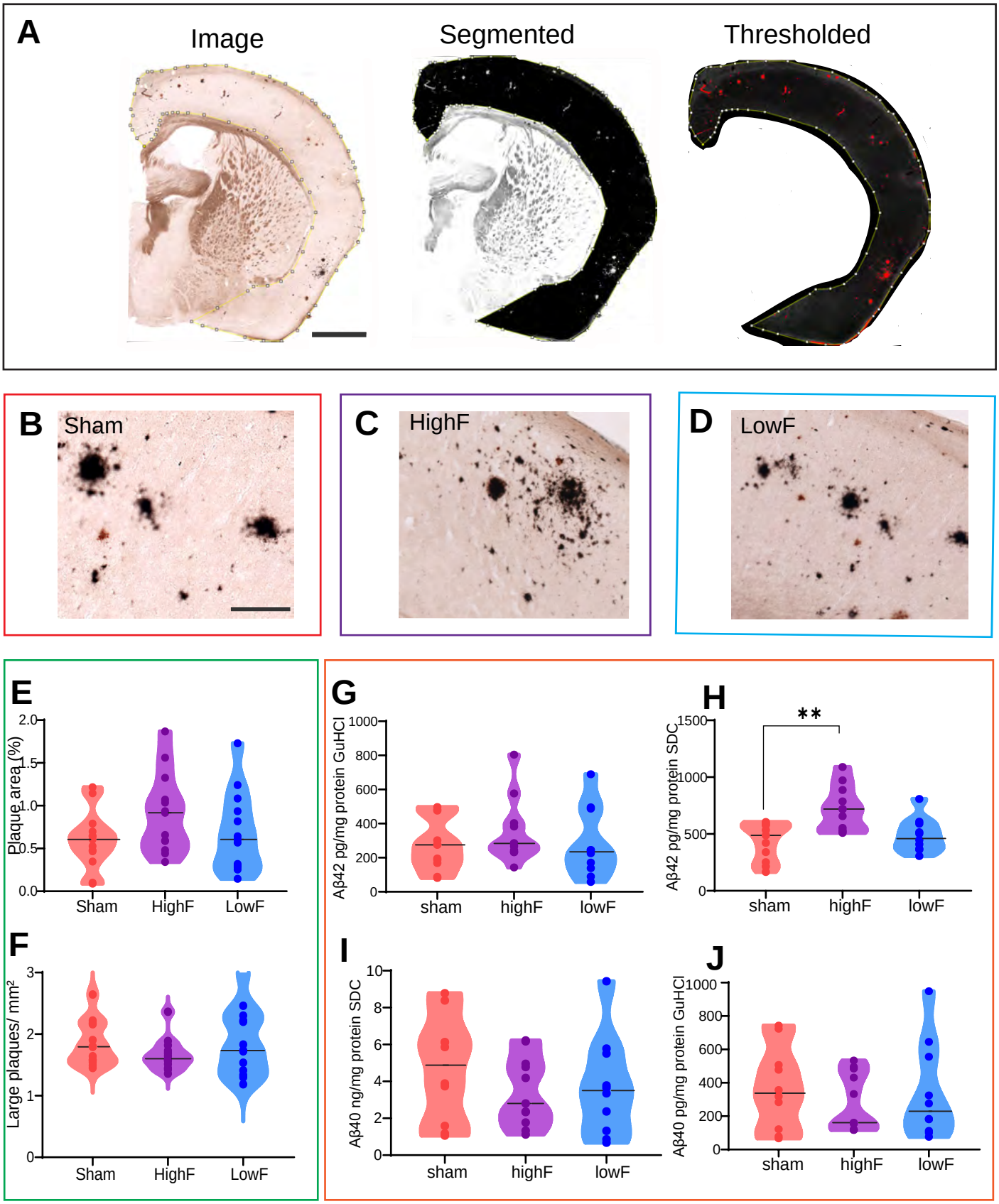
A
Image
Segmented
Thresholded
B
Sham
C
HighF
D
LowF
E
Plaque area (%)
2.0
1.5
1.0
0.5
0.0
Sham
HighF
LowF
F
Large plaques/ mm²
3
2
1
0
Sham
HighF
LowF
G
Aβ42 pg/mg protein GuHCl
1000
800
600
400
200
0
sham
highF
lowF
H
Aβ42 pg/mg protein SDC
1500
1000
500
0
**
sham
highF
lowF
I
Aβ40 ng/mg protein SDC
10
8
6
4
2
0
sham
highF
lowF
J
Aβ40 pg/mg protein GuHCl
1000
800
600
400
200
0
sham
highF
lowF

Figure 4

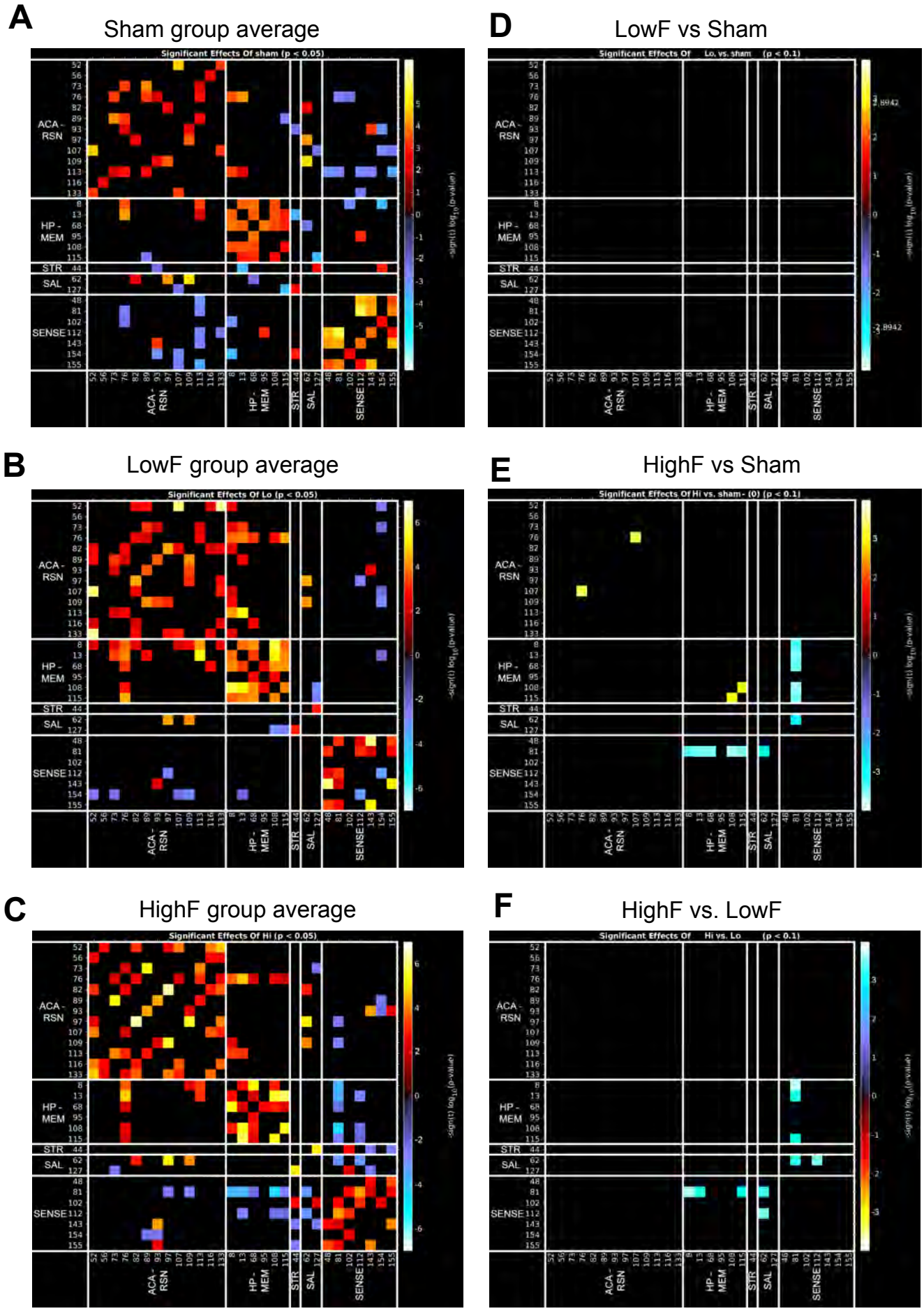
A
Sham group average
Significant Effects Of sham (p < 0.05)
B
LowF group average
Significant Effects Of Lo (p < 0.05)
C
HighF group average
Significant Effects Of Hi (p < 0.05)
D
LowF vs Sham
Significant Effects Of Lo vs. sham (p < 0.1)
E
HighF vs Sham
Significant Effects Of Hi vs. sham - (0) (p < 0.1)
F
HighF vs. LowF
Significant Effects Of Hi vs. Lo (p < 0.1)
ACA - RSN
HP - MEM
STR
SAL
SENSE
-sign(t) log10(p-value)

Figure 5

A

Anaesthesia:	isoflurane		medotomide		
	T2	diffusion MRI	evoked MRI	resting state fMRI	dynamic contrast MRI

B

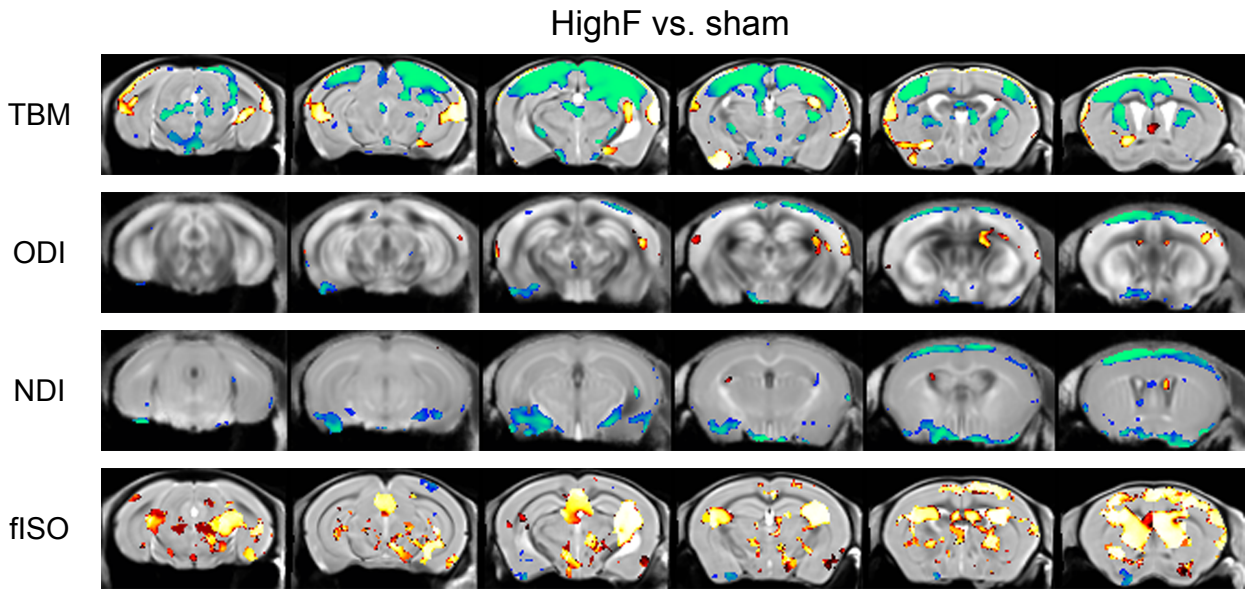

C

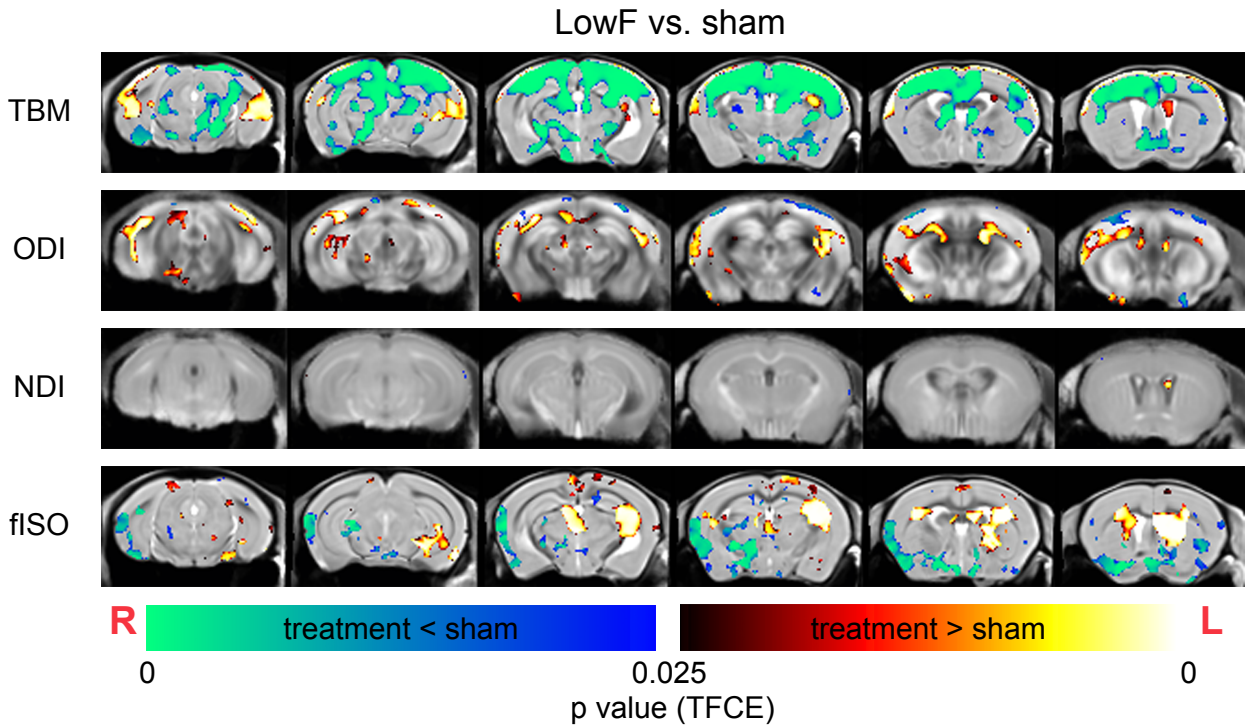

Figure 6

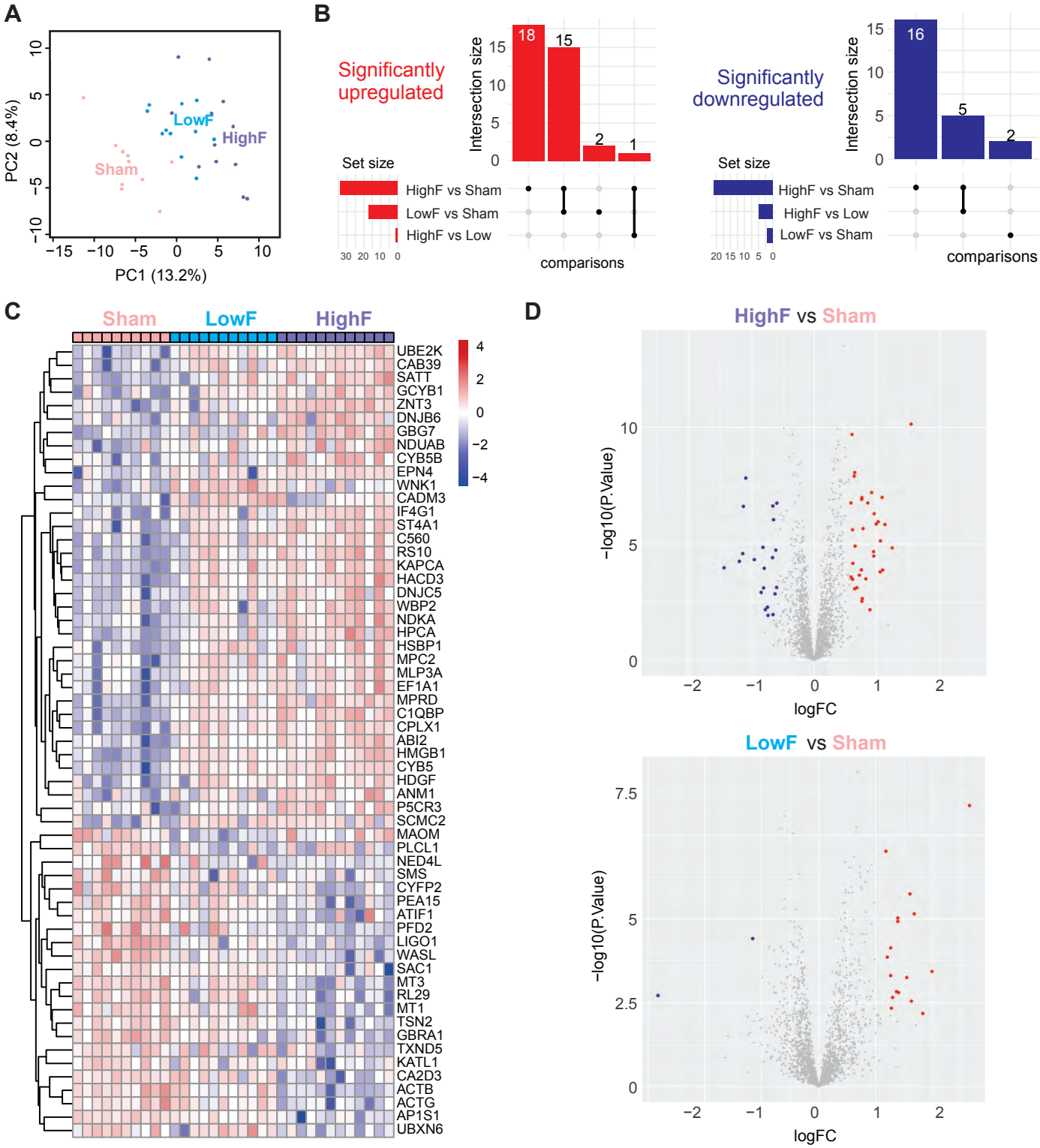
A
PC2 (8.4%)
PC1 (13.2%)
LowF
HighF
Sham
B
Significantly upregulated
Intersection size
Set size
HighF vs Sham
LowF vs Sham
HighF vs Low
comparisons
Significantly downregulated
HighF vs Sham
HighF vs Low
LowF vs Sham
comparisons
C
Sham
LowF
HighF
UBE2K
CAB39
SATT
GCYB1
ZNT3
DNJB6
GBG7
NDUAB
CYB5B
EPN4
WNK1
CADM3
IF4G1
ST4A1
C560
RS10
KAPCA
HACD3
DNJC5
WBP2
NDKA
HPCA
HSBP1
MPC2
MLP3A
EF1A1
MPRD
C1QBP
CPLX1
ABI2
HMGB1
CYB5
HDGF
ANM1
P5CR3
SCMC2
MAOM
PLCL1
NED4L
SMS
CYFP2
PEA15
ATIF1
PFD2
LIGO1
WASL
SAC1
MT3
RL29
MT1
TSN2
GBRA1
TXND5
KATL1
CA2D3
ACTB
ACTG
AP1S1
UBXN6
D
HighF vs Sham
−log10(P.Value)
logFC
LowF vs Sham
−log10(P.Value)
logFC

Figure 7

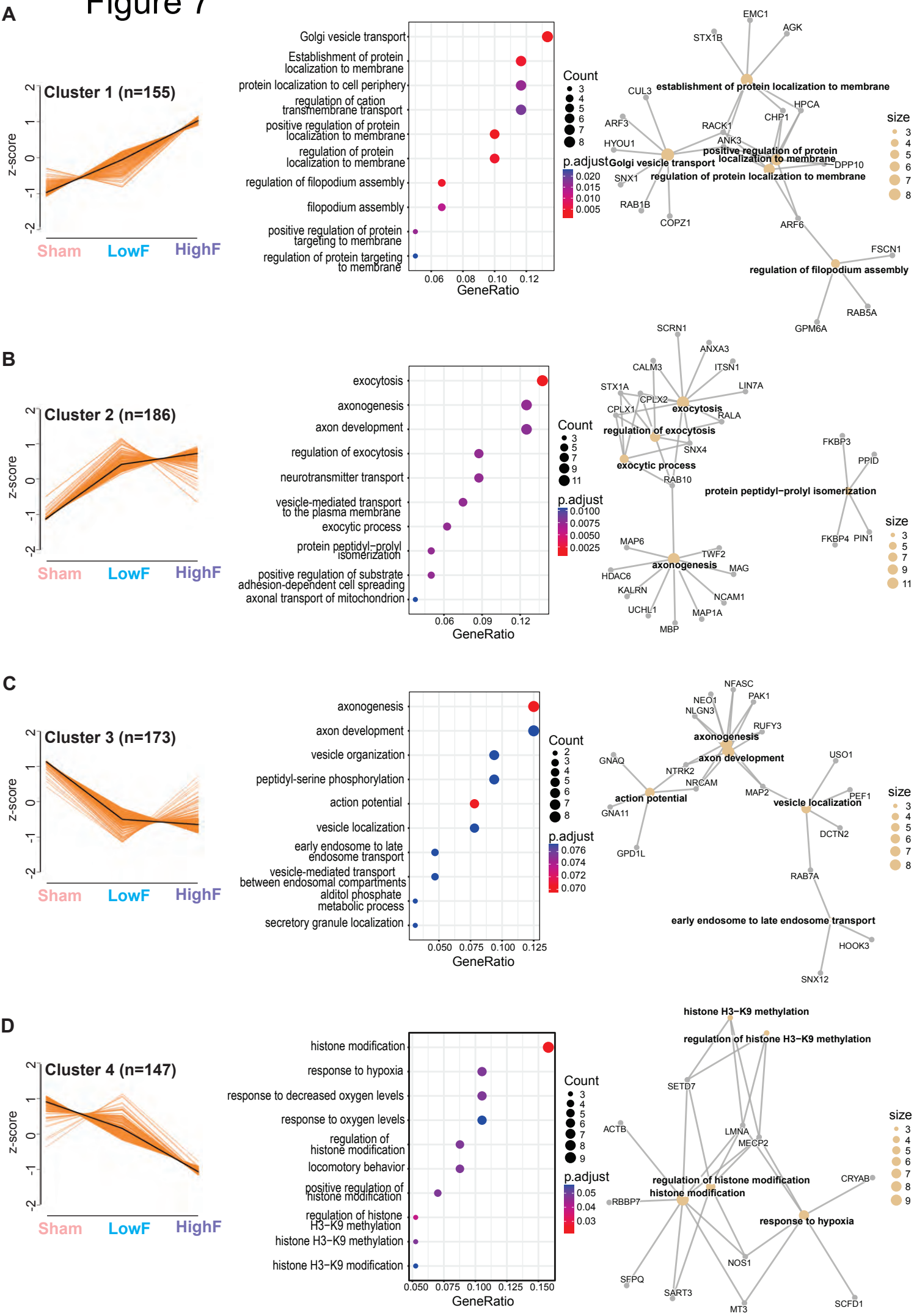
A
Cluster 1 (n=155)
z-score
Sham
LowF
HighF
Golgi vesicle transport
Establishment of protein localization to membrane
protein localization to cell periphery
regulation of cation transmembrane transport
positive regulation of protein localization to membrane
regulation of protein localization to membrane
regulation of filopodium assembly
filopodium assembly
positive regulation of protein targeting to membrane
regulation of protein targeting to membrane
GeneRatio
Count
p.adjust
size
establishment of protein localization to membrane
Golgi vesicle transport
positive regulation of protein localization to membrane
regulation of protein localization to membrane
regulation of filopodium assembly
B
Cluster 2 (n=186)
exocytosis
axonogenesis
axon development
regulation of exocytosis
neurotransmitter transport
vesicle-mediated transport to the plasma membrane
exocytic process
protein peptidyl−prolyl isomerization
positive regulation of substrate adhesion-dependent cell spreading
axonal transport of mitochondrion
C
Cluster 3 (n=173)
axonogenesis
axon development
vesicle organization
peptidyl-serine phosphorylation
action potential
vesicle localization
early endosome to late endosome transport
vesicle-mediated transport between endosomal compartments
alditol phosphate metabolic process
secretory granule localization
D
Cluster 4 (n=147)
histone modification
response to hypoxia
response to decreased oxygen levels
response to oxygen levels
regulation of histone modification
locomotory behavior
positive regulation of histone modification
regulation of histone H3−K9 methylation
histone H3−K9 methylation
histone H3−K9 modification
histone H3−K9 methylation
regulation of histone H3−K9 methylation
regulation of histone modification
histone modification
response to hypoxia

Figure 8

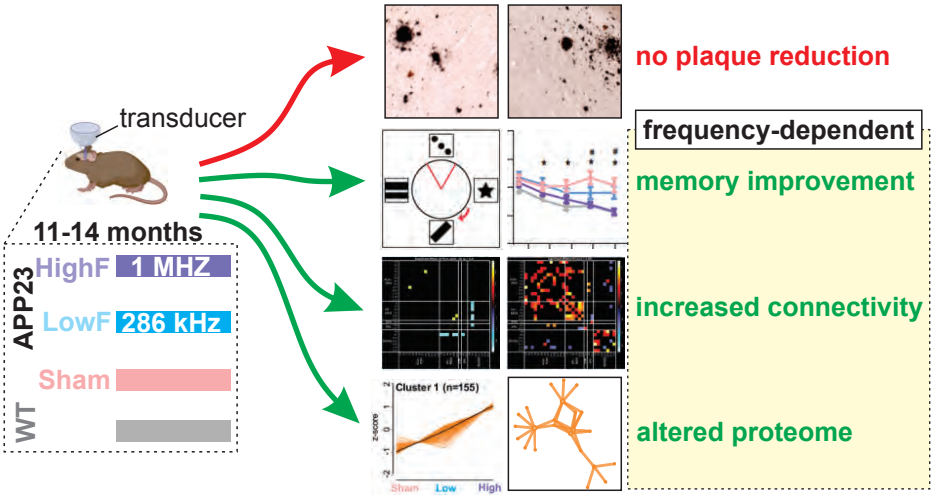
transducer
11-14 months
APP23
HighF
1 MHZ
LowF
286 kHz
Sham
WT
no plaque reduction
frequency-dependent
memory improvement
increased connectivity
altered proteome
Cluster 1 (n=155)
Sham
Low
High